Comparative Study of Large-slip Axial Motion of a Slender Body in Different Tubes

Di Zhang [1], Ke-Dong Zhou[1]*, Lei He [1], Chao Shen [2], Mo Yang [1], Yi-hui Liu [1],
Hai-Yue Ren [1]

[1] School of Mechanical Engineering, Nanjing University of Science and Technology, Nanjing
210094, Jiangsu, China
[2] China Ship Scientific Research Center, Wuxi 214082, Jiangsu, China
*Corresponding author: zkd81151@njust.edu.cn

Abstract. To investigate the influence of different tube on slender body during large-slip axial motion, a coupled finite element model was established and coupled with the VUAMP subroutine. The process of large-slip axial motion of the slender body was then simulated using Abaqus software. The motion states and surface morphologies of slender bodies moving in three tubes, namely an 820mm rectangular tube, an 850mm rectangular tube and an 820mm polygonal tube were compared. The simulation results demonstrate that the slender body of the polygonal tube exhibits faster in-tube motion, little motion disturbance, and more stable motion. Additionally, its horizontal direction centroid offset is only 5% of that of the rectangular tube. Furthermore, the slender body of the polygonal tube exhibits minimal stress-strain characteristics. The surface morphology of the slender body of the polygonal tube is not conspicuous at the valleys and hills boundaries and the scratch grooves of the slender body of the rectangular tube are deep. The above obvious different surface morphologies should result in great influence on aerodynamic parameters.

Keywords: effect of tube on slender body, polygonal tube, rectangular tube, surface morphology

1   Introduction

During the large-slip axial motion process, the tube creates a high-velocity, high-pressure impact on the slender body [1], which affects the motion and the surface morphology of the slender body. In recent years, scholars have conducted a substantial body of research on this. Liu [2] conducted a dynamic large-slip axial motion test of two different slender bodies, and the resistance characteristic curves were obtained. Xu [3] employed the Abaqus software to simulate the dynamic large-slip axial motion process of the slender body and conducted dynamic large-slip axial motion tests to get the parameters of slender body/tube interaction in different cases.

The objective of this paper is to investigate the effects of different tube on slender body and its influencing law by numerical simulation techniques. A coupled finite element model of the slender body/tube was constructed through the explicit dynamics

finite element method. Subsequently, the effects of different structures and various lengths of tubes on the motion and the surface morphologies of the slender bodies are compared.

2 Materials and Methods

2.1 Model Properties

Three slender body/tube geometric models were constructed for three different tubes: 820 mm rectangular tube (designated "rectangular 820"), 850 mm rectangular tube (designated "rectangular 850"), and 820 mm polygonal tube (designated "polygonal 820"). Additionally, a geometric model of the front part of the housing was developed, which was utilized to provide preliminary constraints for the slender body. Furthermore, in this paper, we use the Johnson-Cook model [4].

2.2 Meshing

To circumvent element shear locking, C3D8RTs are used for the tubes, the slender bodis and the housings. Localised mesh densification of the part of the slender body in contact with the tube is employed to meet the requisite calculation accuracy. To ascertain the mesh-independence validation, slender body mesh models with different mesh densities are constructed, with the polygonal tube serving as a case study. Table 1 presents the simulation results.

Table 1. Numerical results of meshes with different densities.

scenario	grid number	$v_0/\text{m}\cdot\text{s}^{-1}$	time/h
1	150k	769.5	5.7
2	220k	798.8	8.1
3	300k	805.4	11.4

Table 1 shows that after increasing the number of grids from 220,000 to 300,000, the computation time increases by 40.7%, but the initial velocity increases by only 0.8%. Scenario 2 can fulfill the requisite accuracy standards while simultaneously exhibiting a high computational efficiency. Consequently, scenario 2 is deemed an optimal choice. The total number of meshes for the polygonal 820 model when meshed using Scheme 2 is approximately 1.6 million. **Fig. 1** illustrates the assembled FEA model of the slender body/tube.
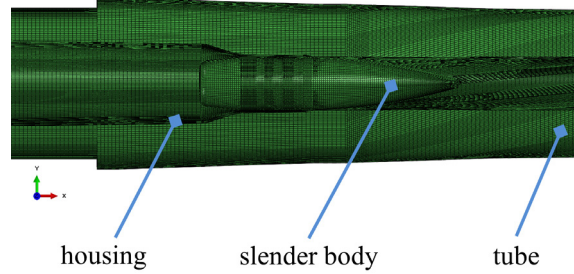
Fig. 1. Assembled FEA model of slender body/tube.

2.3 Constraints and Load Application

The end of the tube and the housing are defined as complete constraints, thereby restraining all of their degrees of freedom. The loads are applied using the VUAMP subroutine coupling calculation approach which is described in the literatures [5-9]. **Fig. 2** illustrates the flowchart of the coupling calculation. Furthermore, the model is subjected to the effects of gravity.
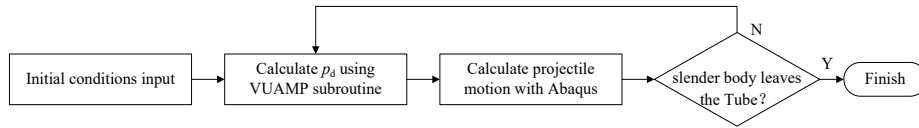

Fig. 2. Flowchart of the coupling calculation.

3 Simulation Results

The origin of the coordinate is designated as O, which is set at the center of the aft end face of the tube. The X-axis is aligned with the direction of the tube, extending to the tube opening, the Y-axis is perpendicular to the X-axis and oriented upwards, and the Z-axis is determined by the right-hand rule.

3.1 A Comparative Analysis of Slender Body Motion

Comparative Analysis of Internal Duration and Initial Velocity. The internal durations of the 820 rectangular model, 850 rectangular model and 820 polygonal model are 1.82ms, 1.87ms and 1.81ms, respectively, and the initial velocities are 787.30m/s, 795.04m/s and 798.80m/s, respectively, indicating that the slender body moves faster inside the polygonal tube.

Comparative Analysis of Offsets of the Centroid of Slender Body in the OYZ Plane. When the slender body is moving, its centroid oscillates in the OYZ plane. The offsets of the centroid of slender body are shown in **Fig. 3**.

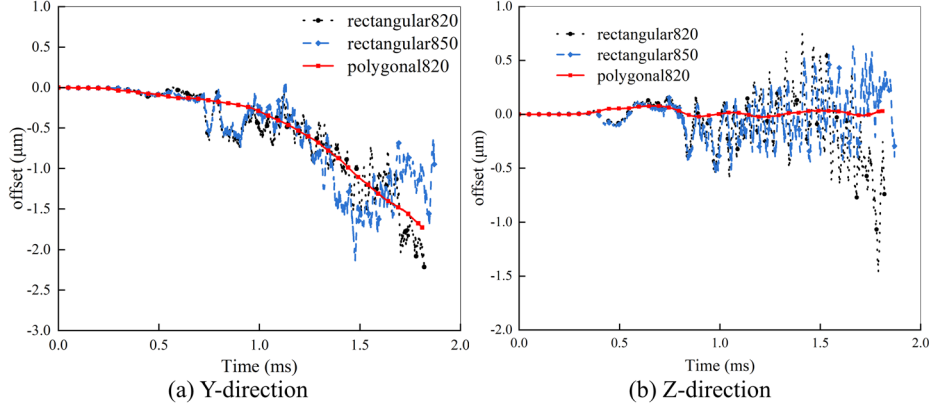|	
(a) Y-direction	(b) Z-direction

Fig. 3. Offsets curves of centroid.

At the beginning of the curve, the offset of the centroid of the slender body in the Y- and Z-axis directions is approximately equal to 0. This is due to the constraints imposed by the housing. After that, the offsets gradually increased, and the oscillation phenomenon began to appear. It is also evident that there is a greater offset in the Y-axis and that the Y-axis offset gradually increases over time due to the gravitational load applied in the negative direction in the Y-axis. In addition, at the end of the curve, the centroid oscillation of the slender body is greater for the 820 rectangular tube than for the 850 rectangular tube, due to the longer tube of the 850 rectangular tube, resulting in a longer retention period of the slender body, a higher rotational speed and relative stability.

Moreover, it can be seen that the amplitude of the oscillation of the centroid of the slender body of the polygonal tube is smaller than that of the rectangular tube. In the Y-axis direction, due to the superposition of the effect of gravity, the maximum offsets of the centroid of the slender body of the rectangular and polygonal tube are 2.22 μm and 1.73 μm, respectively, and the maximum offset of the centroid of the slender body of the rectangular tube is 1.28 times of that of the polygonal tube, but in the Z-axis direction, the maximum offsets of the centroid of the slender body of the rectangular and polygonal tube are 1.46 μm and 0.07 μm, respectively. The maximum offset of the centroid of the slender body of rectangular tube is 20.86 times of that of the polygonal tube. The above results show that the slender body movement in the polygonal tube is smoother than that in the rectangular tube.

Comparative Analysis of Slender Body Rotational Velocity. The theoretical value of the initial rotational velocity of the slender body is given by equation(1) [10]:

$$\omega_0 = \frac{2\pi v_0}{\eta d} \tag{1}$$

where ω_0 is the initial rotational velocity of the slender body, v_0 is the initial velocity, η is the pitch, and d is the diameter.

Table 2 presents a comparison of the slender body rotational velocities of the three models. The errors between the simulated and theoretical values in the table are less than 4%, which proves the accuracy of the simulation.

Table 2. Results of slender body rotational velocity.

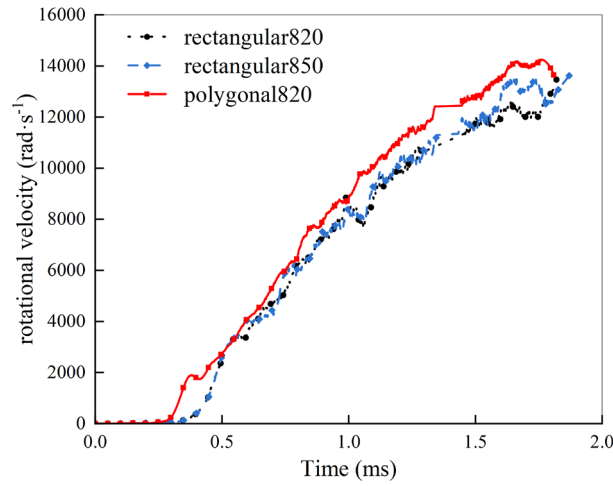| model	rotational velocity /rad·s⁻¹		Inaccuracies/%
	theoretical	simulated	
rectangular 820	13018	13465	3.43
rectangular 850	13146	13620	3.61
polygonal 820	13199	13643	3.36

Fig. 4. Slender body rotational velocity-time curves.

Fig. 4 illustrates the slender body rotational velocity-time curves for the three models by simulation. The curves for the three models exhibit a consistent trend. In the initial phase of the slender body's trajectory, the rotational velocities of the three models are estimated to be approximately zero. This is because the slender body has not yet interacted with the tube. Subsequently, the slender body commences a rotational movement as a consequence of the tube. Furthermore, the polygonal tube exhibits a slightly faster rotational velocity than the rectangular tube, and the simulated values of the two are 13,643 rad/s and 13,465 rad/s, respectively, with a difference of 178 rad/s (about 1.3%). The oscillation of the rotational velocity data is lower. These results demonstrate that the polygonal tube has superior rotational stability.

3.2 A Comparative Analysis of Slender Body Stress-strain

The slender body stress nephograms obtained from the simulation of the three models are presented in **Fig. 5**, and the strain nephograms are presented in **Fig. 6**.
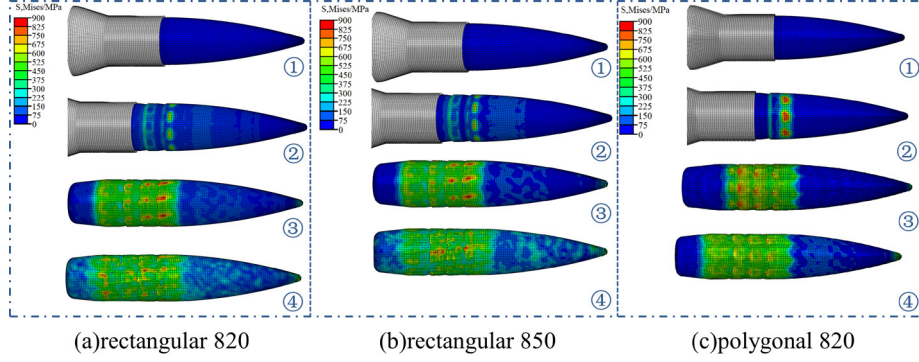
(a)rectangular 820   (b)rectangular 850   (c)polygonal 820

Fig. 5. Stress nephograms.

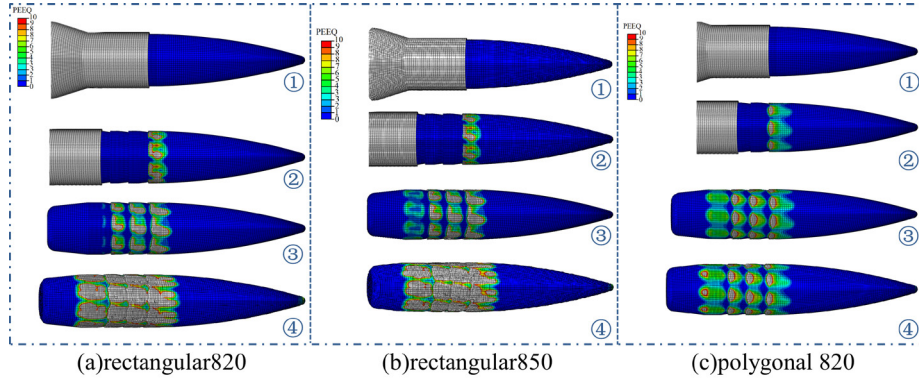(a)rectangular820   (b)rectangular850   (c)polygonal 820

Fig. 6. Strain nephograms.

  The slender bodies have undergone four distinct moments. In the initial moment (①), the slender body is fully constrained by the housing. In the second moment (②), the slender body begins to move. At this moment, the front end of the cylindrical part of the slender body begins to be constrained by the tube, while the rear end remains subjected to the constraints of the housing. In the third moment (③), the slender body has been completely released from the constraints of the housing. However, the engraving process is not yet completed, and the cylindrical part of the slender body only be constrained by the tube, while the rear end remains free. This state can potentially cause instability in the movement of the slender body. In the fourth moment (④), the slender body is completely engraved into the tube and begins to move along in-tube. Moreover, the stress-strain of the slender body of the polygonal tube is significantly smaller than that of the rectangular tube, indicating that the stress environment of the rectangular tube is worse than that of the polygonal tube.

3.3   A Comparative Analysis of Slender Body Surface Morphology

After the engraving process, the slender body surface morphologies of the three models are illustrated in **Fig. 7**.

hill   valley   hill   valley   hill   valley
(a)rectangular820   (b)rectangular850   (c)polygonal 820
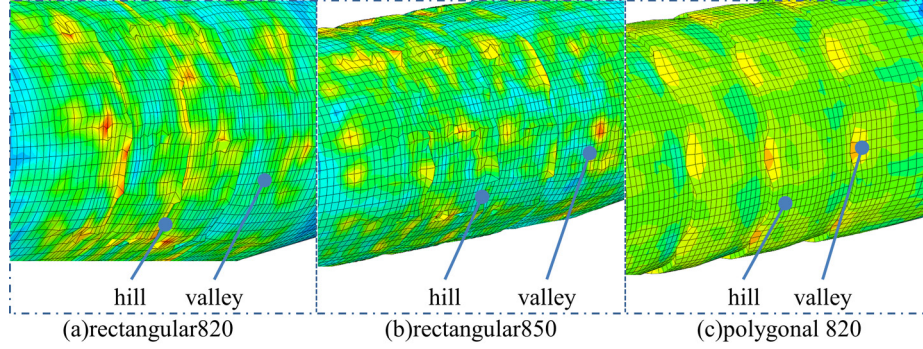
Fig. 7. Surface morphologies of slender bodies.

The slender body surface valleys caused by the rectangular tube are evident, manifesting as trapezoidal-like valleys. In contrast, the slender body valleys caused by the polygonal tube are less pronounced, with a relatively gradual transition between the hills and the valleys. It is known from aerodynamics that the differences in the morphologies of the slender bodies caused by the rectangular and polygonal tubes will cause differences in the aerodynamic parameters of the slender bodies [11].

4   Conclusions

In this paper, we investigate the influence law of different tubes on the slender bodies. The following conclusions are thus obtained:

(1) A slender body of a polygonal tube has a high velocity of movement and its centroid is less disturbed during the movement, making the movement more stable than that of a slender body of a rectangular tube.

(2) The slender bodies of the three models have undergone four moments, which can be defined as follows: the initial stationary moment, the beginning of engraving with housing constraint moment, incomplete engraving without housing constraint moment, and the completion of engraving moment. In these four moments, the in-tube stress environment of the rectangular tube is more severe than that of the polygonal tube.

(3) The rectangular tube forms a trapezoidal-like indentation on the slender body surface, and the boundaries of the hills and valleys are distinctly visible and the polygonal tube exhibits minimal plastic deformation on the slender body surface, and the boundaries of the hills and valleys are not readily discernible. Additionally, the differences in the morphologies of the slender bodies caused by the rectangular and polygonal tubes will cause differences in the aerodynamic parameters of the slender bodies.

References

1. Yang, Y. Z., Zhang, X. Y., Xu, C. (2020) The interaction between copper Jacket projectile and barrel under different temperature based on thermo-mechanical coupling finite element model[J]. Journal of Vibration and Shock, 39(10): 44-51. DOI: 10.13465/j.cnki.jvs.2020.10.006.
2. Liu, D. Y., Sun, P., Zhang, X. W., et al. (2020) Experimental study on engraving resistance properties of band of two medium caliber projectile[J]. Journal of Ballistics, 32(03): 5-8. DOI: 10.12115/j.issn.1004-499X (2020) 03-002
3. Xu, H., Huang, C L., Wang, X. K., et al. (2022) Theoretical and experimental study of projectile dynamic engraving resistance[J]. Acta Armamentarii, 43(9): 2263-2273. DOI: 10.12382/bgxb.2021.0875
4. Johnson, G. R., Cook, W. H. (1985) Fracture characteristics of three metals subjected to various strains, strain rates, temperatures and pressures[J]. Eng Fract Mech, 21: 31e48. DOI: 10.1016/0013-7944(85)90052-9
5. Wang, S. Q, Li, Q., Fan, J. T., et al. (2024) Analysis of the dynamic characteristics of a small caliber gun's bullet engraving process[J]. Journal of Vibration and Shock, 43(12): 241-247. DOI: 10.13465/j.cnki.jvs.2024.12.027
6. Fan, J. T., Li, Q., Ran, X. C., et al. (2023) Simulation study on the influence of slope bore processing error on internal ballistic performance［J］. Journal of Ordnance Equipment Engineering, 44(12)：220-226. DOI: 10.11809/bqzbgcxb2023.12.029
7. Xu, H. (2023) Study on dynamic characteristics of cased telescoped ammunition during engraving process[D], Doctoral Dissertation of Nanjing University of Science and Technology.
8. Shen, C., Zhou, K. D., Lu, Y., et al. (2019) Modeling and simulation of bullet-barrel interaction process for the damaged gun barrel[J]. Defence Technology, 15(6): 972-986. DOI: 10.1016/j.dt.2019.07.009.
9. Shen, C., Zhou, K. D., Lu, Y., et al. (2018) Research on the influence of aamaged bore of a large caliber machine gun on bullet engraving progress[J]. Acta Armamentarii, 39(12): 2320-2329. DOI: 10.3969/j.issn.1000-1093.2018.12.005
10. Wu, Z. L., Li, Z. X., Liu, K., et al. (2020) Ammunition of automatic weapon[M]. Beijing: Beijing Institute of Technology Press.
11. Zhao, L.，Dong, F. Q. (2015) Analysis about rifling grooves of small-caliber ammunition on the flow field[J]. Journal of Projectiles, Rockets, Missiles and Guidance, 35(2): 126-128, 133. DOI: 10.15892/j.cnki.djzdxb.2015.02.032.